

Multifunctional Hyperuniform Cellular Networks: Optimality, Anisotropy and Disorder

S. Torquato

Department of Chemistry, Department of Physics, Princeton Institute for the Science and Technology of Materials, and Program in Applied and Computational Mathematics, Princeton University, Princeton, New Jersey 08544, USA

E-mail: torquato@electron.princeton.edu

D. Chen

Department of Chemistry, Princeton University, Princeton, New Jersey 08544, USA

Abstract. Disordered hyperuniform heterogeneous materials are new, exotic amorphous states of matter that behave like crystals in the manner in which they suppress volume-fraction fluctuations at large length scales, and yet are statistically isotropic with no Bragg peaks. It has recently been shown that disordered hyperuniform dielectric two-dimensional cellular network solids possess complete photonic band gaps comparable in size to photonic crystals, while at the same time maintaining statistical isotropy, enabling waveguide geometries not possible with photonic crystals. Motivated by these developments, we explore other functionalities of various two-dimensional ordered and disordered hyperuniform cellular networks, including their effective thermal or electrical conductivities and elastic moduli. We establish the multifunctionality of a class of such low-density networks by demonstrating that they maximize or virtually maximize the effective conductivities and elastic moduli. This is accomplished using the machinery of homogenization theory, including optimal bounds and cross-property bounds, and statistical mechanics. We rigorously prove that anisotropic networks consisting of sets of intersecting parallel channels in the low-density limit, ordered or disordered, possess optimal effective conductivity tensors. For a variety of different disordered networks, we show that when short-range and long-range order increases, there is an increase in both the effective conductivity and elastic moduli of the network. Moreover, we demonstrate that the effective conductivity and elastic moduli of various disordered networks derived from disordered “stealthy” hyperuniform point patterns possess virtually optimal values. We note that the optimal networks for conductivity are also optimal for the fluid permeability associated with slow viscous flow through the channels as well as the mean survival time associated with diffusion-controlled reactions in the channels. In summary, we have identified ordered and disordered hyperuniform low-weight cellular networks that are multifunctional with respect to transport (e.g., heat dissipation and fluid transport), mechanical and electromagnetic properties, which can be readily fabricated using 3D printing and lithographic technologies.

1. Introduction

Heterogeneous materials consisting of different phases are ideally suited to achieve a broad spectrum of desirable bulk physical properties by combining the best features of the constituents through the strategic spatial arrangement of the different phases [1–5]. Multifunctional cellular network solids are commonly used in many applications due to their light weight and desirable transport, mechanical, optical and acoustic properties [6–19]. For example, cellular solids are used as structural panels, energy adsorption devices and thermal insulators [6–8].

Motivated by the hyperuniformity concept that enables a unified classification of ordered and special disordered structures [20–22], this paper explores the multifunctionality of cellular networks with varying degrees of order (or disorder). The hyperuniformity notion was first introduced in the context of many-particle systems more than a decade ago [20]. Hyperuniform many-particle systems have density fluctuations that are anomalously suppressed at long wavelengths compared to those in typical disordered point configurations, such as ideal gases, liquids, and glasses [20, 21]. More precisely, a many-particle system is hyperuniform if its structure factor $S(\mathbf{k})$ [defined in Eq. (1)] tends to zero as the wavenumber $k \equiv |\mathbf{k}|$ goes to zero (where \mathbf{k} is the wavevector). Hyperuniform systems include all perfect crystals and quasicrystals, and special disordered varieties [20, 21]. Disordered hyperuniform many-particle systems are amorphous states of matter that lie between a crystal and a liquid: they behave like crystals in the way that they suppress density fluctuations at very large length scales, and yet they are statistically isotropic with no Bragg peaks. In this sense, they have a *hidden* long-range order that is not visually apparent [20, 21] (see Sec. 2 for precise definitions).

The concept of hyperuniformity was generalized to two-phase materials [21, 23–25]. A hyperuniform two-phase medium is one in which the local volume-fraction fluctuations are suppressed at large length scales. More precisely, a two-phase system is hyperuniform if its spectral density $\tilde{\chi}_V(\mathbf{k})$ (defined in Sec. 2) tends to zero as k goes to zero. Clearly, any network can be viewed as two-phase medium consisting of a “channel” phase distributed throughout some matrix or void phase. Recently, disordered hyperuniform two-phase materials were found to possess desirable transport and mechanical properties, and wave-propagation characteristics [25–27].

Disordered “stealthy” hyperuniform dielectric two-dimensional networks [28, 29] are novel cellular solids that have recently been shown to possess complete photonic band gaps comparable in size to photonic crystals, while at the same time maintaining statistical

isotropy, enabling waveguide geometries not possible with photonic crystals [28, 29]. Stealthy patterns are not only hyperuniform but they possess zero-scattering intensity for a range of wavenumbers around the origin (see Sec. 2 for a precise definition). Disordered stealthy hyperuniform materials can be thought of as an exotic state of matter intermediate between a crystal and a liquid [22]. This photonic study provides a vivid example of a class of disordered materials that has advantages over ordered counterparts and has led to a flurry of papers on the study of photonic properties of disordered hyperuniform networks [30–34]. It has been suggested [22] that the novel properties associated with disordered stealthy networks is related to the fact that they cannot possess arbitrarily large “holes” (or cells) [35]. In addition, disordered stealthy hyperuniform two-phase materials were recently found to possess desirable transport properties [25, 26].

Motivated by these developments, we explore other functionalities of various two-dimensional ordered and disordered hyperuniform cellular networks in the low-density limit, including their effective thermal or electrical conductivities and elastic moduli. Our overall objective is to investigate how hyperuniformity affects the effective conductivity and elastic moduli of the networks, and how close disordered hyperuniform networks, under the constraint of isotropy, can come to being optimal, i.e., maximal with respect to these physical properties. We establish the multifunctionality of a class of such networks by demonstrating that they maximize or virtually maximize the effective conductivities and elastic moduli. This is accomplished using the machinery of homogenization theory, including optimal bounds and cross-property bounds, and statistical mechanics. By mathematical analogy, all of our results for the effective conductivity apply as well to the effective dielectric constant and effective magnetic permeability [1]. In addition, our results for the effective conductivity are also optimal for the fluid permeability and mean survival time (see Sec. 7 for details).

For purposes of comparison, we first investigate the effective properties of ordered (periodic) hyperuniform networks, which include both macroscopically isotropic and anisotropic varieties †. Then we study various disordered networks that are statistically isotropic derived from Voronoi, Delaunay, and what we term as “Delaunay-centroidal” tessellations derived from hyperuniform and nonhyperuniform point patterns. We employ theoretical and simulation techniques, rigorous bounds, and cross-property bounds to determine the effective conductivity and elastic mod-

† Macroscopic anisotropy refers to an anisotropic effective property tensor. Macroscopic isotropy refers to an isotropic effective property tensor.

uli of the networks. To quantify how close the effective conductivity tensor of an anisotropic network is to being optimal (i.e., maximal), we introduce and compute the *tortuosity* tensor τ .

We rigorously demonstrate for the first time that anisotropic networks consisting of sets of intersecting parallel channels possess optimal effective conductivity tensors. It is noteworthy that this proof applies to disordered hyperuniform and nonhyperuniform varieties, where the parallel channels in each set are not equally spaced. We generally find that when short-range and long-range order of a Voronoi, Delaunay, or “Delaunay-centroidal” network increases, there is an increase in both the effective conductivity and bulk moduli of the network, and the shear moduli in the cases of Delaunay networks. Moreover, we demonstrate that the effective conductivity and bulk moduli of certain disordered networks derived from disordered stealthy hyperuniform point patterns, and the shear moduli of certain Delaunay networks possess virtually optimal values.

The rest of the paper is organized as follows: in Sec. 2, we provide key definitions and preliminary discussion. In Sec. 3, we briefly review basic results from homogenization theory that are applied in this paper. In Sec. 4, we apply the general homogenization theory to low-density network solids and derive specific results for these structures. In Sec. 5, we determine the effective conductivity and elastic moduli for various periodic hyperuniform networks, and compute the tortuosity tensors of these networks. We also provide a rigorous proof that networks consisting of intersecting parallel channels possess optimal effective conductivity. In Sec. 6, we determine the effective conductivity and elastic moduli for various disordered hyperuniform and nonhyperuniform networks. In Sec. 7, we discuss the results and provide concluding remarks.

2. Definitions And Preliminaries

2.1. Point Patterns

A statistically homogeneous point pattern in d -dimensional Euclidean space \mathbb{R}^d at number density ρ is characterized by its n -particle correlation function g_n [1]. A periodic point pattern represents a special subset of point patterns. It is obtained by placing a fixed configuration of N points (where $N \geq 1$) within one fundamental cell (the smallest repeating unit), which is then periodically replicated [36].

Often in practice only lower-order statistics are available for statistically homogeneous point patterns. The pair correlation function $g_2(\mathbf{r})$ is a particularly important quantity, which is defined to be proportional to the probability of finding a point at a displacement of \mathbf{r} away from a given reference point [1]. The

structure factor $S(\mathbf{k})$ is essentially related to the Fourier transform of $g_2(\mathbf{r})$; specifically, it is given in terms of the Fourier transform $\tilde{h}(\mathbf{k})$ of total correlation function $h(\mathbf{r}) \equiv g_2(\mathbf{r}) - 1$ [1] via

$$S(\mathbf{k}) = 1 + \rho \tilde{h}(\mathbf{k}), \quad (1)$$

where \mathbf{k} is the wave vector.

A hyperuniform many-particle system in d -dimensional Euclidean space \mathbb{R}^d at number density ρ is one in which the structure factor $S(\mathbf{k})$ tends to zero as the wavenumber $k \equiv |\mathbf{k}|$ tends to zero [20, 21], i.e.,

$$\lim_{|\mathbf{k}| \rightarrow 0} S(\mathbf{k}) = 0. \quad (2)$$

Equivalently, the local number density fluctuation $\sigma_N^2(R)$ associated with a spherical window of radius R of hyperuniform systems grows more slowly than the volume of that window [20], i.e., slower than R^d . Stealthy systems are a special hyperuniformity class in which the structure factor is identically zero for a range of wavenumbers around the origin, i.e.,

$$S(\mathbf{k}) = 0 \quad \text{for } 0 \leq |\mathbf{k}| < K, \quad (3)$$

where the constant K is the radius of the “exclusion sphere”. The “stealthiness” parameter

$$\chi = \frac{M(k)}{d(N-1)}, \quad (4)$$

which is inversely proportional to the number density, gives a measure of the relative fraction of constrained degrees of freedom compared to the total number of degrees of freedom $d(N-1)$ (subtracting out the system translational degrees of freedom) [37]. Here $M(k)$ is the number of independently constrained wave vectors in the exclusion region, and N is the number of points in the system [37]. For $0 \leq \chi < 1/2$, the ground states are highly degenerate and overwhelmingly disordered [38, 39]. Moreover, short-range order (tendency for particles to repel one another) increases as χ increases; at $\chi = 1/2$, the entropically favored ground states undergo a transition from disordered states to crystalline states [38, 39].

2.2. Two-phase Materials

A two-phase random medium is a domain of space V in \mathbb{R}^d that is partitioned into two disjoint regions: a phase 1 region V_1 and a phase 2 region V_2 such that $V_1 \cup V_2 = V$ [1]. The microstructure of a random two-phase medium is uniquely determined by the indicator functions $\mathcal{I}^{(p)}(\mathbf{x})$ associated with the two individual phases ($p = 1, 2$) defined as

$$\mathcal{I}^{(p)}(\mathbf{x}) = \begin{cases} 1, & \mathbf{x} \text{ in phase } p, \\ 0, & \text{otherwise,} \end{cases} \quad (5)$$

For statistically homogeneous two-phase materials where there are no preferred centers, the two-point probability function $S_2^{(p)}(\mathbf{r})$ measures the probability of finding two points separated by vector displacement \mathbf{r} in phase p [1]. The autocovariance function $\chi_v(\mathbf{r})$ is trivially related to $S_2^{(p)}(\mathbf{r})$ via

$$\chi_v(\mathbf{r}) \equiv S_2^{(p)}(\mathbf{r}) - \phi_p^2, \quad (6)$$

where ϕ_p is the volume fraction of phase p [1]. The spectral density $\tilde{\chi}_v(\mathbf{k})$ is the Fourier transform of the autocovariance function $\chi_v(\mathbf{r})$, where \mathbf{k} is the wavevector. The spectral density $\tilde{\chi}_v(\mathbf{k})$ can be viewed as the counterpart of $S(\mathbf{k})$ in the two-phase context.

A hyperuniform two-phase medium in d -dimensional Euclidean space \mathbb{R}^d is one in which the spectral density $\tilde{\chi}_v(\mathbf{k})$ tends to zero as the wavenumber k tends to zero [21], i.e.,

$$\lim_{|\mathbf{k}| \rightarrow 0} \tilde{\chi}_v(\mathbf{k}) = 0. \quad (7)$$

Equivalently, the local volume-fraction fluctuation $\sigma_v^2(R)$ associated with a spherical window of radius R of hyperuniform media decay more rapidly than the inverse of the volume of window, i.e., faster than R^{-d} , while typical disordered two-phase media have R^{-d} decay [23, 40]. Specifically, in the case of disordered hyperuniform two-phase media, the spectral density $\tilde{\chi}_v(\mathbf{k})$ tends to zero in the limit $|\mathbf{k}| \rightarrow 0$ with the power-law form [21]

$$\tilde{\chi}_v(\mathbf{k}) \sim |\mathbf{k}|^\gamma, \quad (8)$$

where γ is a positive exponent ($\gamma > 0$). Note that the magnitude of γ provides a rough measure of short-range order in the system; as γ tends to infinity, the systems tend towards stealthy two-phase media in which $\tilde{\chi}_v(\mathbf{k})$ is identically zero for a range of wavenumbers around the origin, i.e.,

$$\tilde{\chi}_v(\mathbf{k}) = 0 \quad \text{for} \quad 0 \leq |\mathbf{k}| < K. \quad (9)$$

2.3. Tessellations

We map point patterns in two-dimensional Euclidean space \mathbb{R}^2 into two-dimensional (2D) cellular network structure by using different types of tessellations of the space into polygonal cells based on the underlying patterns. Then we decorate the edges of the resulting polygons in the tessellations with infinitely thin conducting elastic “channels”, as schematically shown in Fig. 1. Specifically, we consider three types of tessellations: Delaunay, Voronoi, and “Delaunay-centroidal” tessellations subject to periodic boundary conditions [28]. A Voronoi cell is the region of space closest to a point than to any other point in the underlying patterns [1]. A Voronoi tessellation is a tessellation of the space by the Voronoi cells. The

Delaunay tessellation is the dual graph of the Voronoi tessellation. The Delaunay-centroidal tessellation is generated by connecting the centroids of the neighboring triangles (which share a common edge) in the Delaunay tessellation [28].

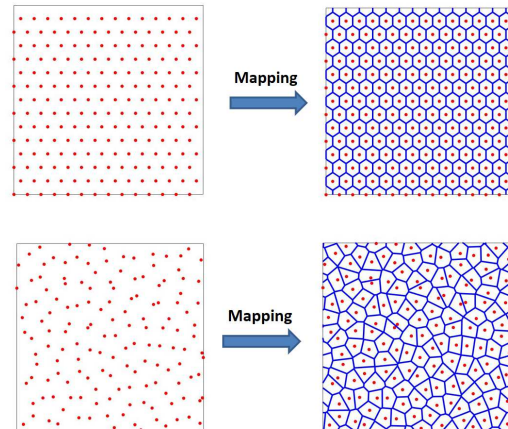


Figure 1. Schematic illustrations that demonstrate the process of mapping point patterns into networks subject to periodic boundary conditions, including one ordered example (top row) and one disordered example (bottom row). Specifically, we partition the space by using certain tessellations of the space based on certain point patterns and then decorate the edges of the resulting polygons in the tessellations with infinitely thin conducting “channels”. In the top row, an ordered point pattern of triangular lattice is mapped into a honeycomb network via Voronoi tessellation, and in the bottom row, a disordered stealthy point pattern is mapped into a disordered network via Voronoi tessellation.

3. Basic Results of Homogenization Theory

Here we collect basic results from homogenization theory of heterogeneous media that are central to this paper. This includes strong-contrast expansions, generalized optimal Hashin-Shtrikman structures for anisotropic media, rigorous effective conductivity bounds and cross-property bounds between the effective conductivity and effective elastic moduli.

3.1. Local and Homogenized Equations

Consider a large two-phase system in d -dimensional Euclidean space \mathbb{R}^d composed of two isotropic phases with electrical (or thermal) conductivities σ_1 and σ_2 . Ultimately, we will take the infinite-volume limit. The local scalar conductivity $\sigma(\mathbf{x})$ at position \mathbf{x} is expressible as

$$\sigma(\mathbf{x}) = \sigma_1 \mathcal{I}^{(1)}(\mathbf{x}) + \sigma_2 \mathcal{I}^{(2)}(\mathbf{x}), \quad (10)$$

where $\mathcal{I}^{(p)}(\mathbf{x})$ is the indicator function for phase p ($p = 1, 2$) defined in Eq. (5). The local constitutive

relation, Ohm's law in the case of electrical conduction or Fourier's law in the case of thermal conduction, is given by

$$\mathbf{J}(\mathbf{x}) = \sigma(\mathbf{x})\mathbf{E}(\mathbf{x}), \quad (11)$$

where $\mathbf{J}(\mathbf{x})$ and $\mathbf{E}(\mathbf{x})$ denote the local flux vector and field (equal to the negative of the gradient of the potential), respectively. Under steady-state conditions, the local flux and field respectively satisfy the divergence-free and curl-free relations:

$$\nabla \cdot \mathbf{J}(\mathbf{x}) = 0. \quad (12)$$

$$\nabla \times \mathbf{E}(\mathbf{x}) = 0. \quad (13)$$

Using homogenization theory [1, 41], it can be shown that the effective electric (or thermal) conductivity second-rank tensor σ_e is determined by the averaged Ohm's (or Fourier's) law:

$$\langle \mathbf{J}(\mathbf{x}) \rangle = \sigma_e \langle \mathbf{E}(\mathbf{x}) \rangle, \quad (14)$$

where angular brackets denote an ensemble average, $\langle \mathbf{J}(\mathbf{x}) \rangle$ is the average flux and $\langle \mathbf{E}(\mathbf{x}) \rangle$ is the average field.

3.2. Exact Contrast Expansions

Consider a macroscopically anisotropic composite medium consisting of two isotropic phases with conductivities σ_p and σ_q ($p \neq q$ with $p = 1, 2, q = 1, 2$) that is characterized by an effective conductivity tensor σ_e . A "strong-contrast" expansion for σ_e was derived in Ref. [42] that perturbs around the generalized optimal Hashin-Shtrikman structures for anisotropic media [1]:

$$\beta_{pq}^2 \phi_p^2 \{\sigma_e - \sigma_q \mathbf{I}\}^{-1} \cdot \{\sigma_e + (d-1)\sigma_q \mathbf{I}\} = \phi_p \beta_{pq} \mathbf{I} - \sum_{n=2}^{\infty} \mathbf{A}_n^{(p)} \beta_{pq}^n \quad (15)$$

where the n -point tensor coefficients $\mathbf{A}_n^{(p)}$ are certain integrals over the $S_n^{(p)}$ associated with phase p and \mathbf{I} is the identity tensor and

$$\beta_{pq} = \frac{\sigma_p - \sigma_q}{\sigma_p + (d-1)\sigma_q}. \quad (16)$$

For $n = 2$,

$$\mathbf{A}_2^{(p)} = \frac{d}{\Omega(d)} \int_{\epsilon} d^2 \mathbf{t}(1, 2) \left[S_2^{(p)}(1, 2) - \phi_p^2 \right], \quad (17)$$

and for $n \geq 3$,

$$\mathbf{A}_n^{(p)} = \left(\frac{-1}{\phi_p} \right)^{n-2} \left(\frac{d}{\Omega(d)} \right)^{n-1} \int d^2 \dots \int dn \mathbf{t}(1, 2) \cdot \mathbf{t}(2, 3) \dots \mathbf{t}(n-1, n) \Delta_n^{(p)}(1, \dots, n), \quad (18)$$

where

$$\mathbf{t}(\mathbf{r}) = \frac{d\mathbf{n}\mathbf{n} - \mathbf{I}}{r^d} \quad (19)$$

is the dipole-dipole tensor,

$$\Omega(d) = \frac{d\pi^{d/2}}{\Gamma(1 + d/2)} \quad (20)$$

is the total solid angle contained in a d -dimensional sphere, and

$$\Delta_n^{(p)} = \begin{vmatrix} S_2^{(p)}(1, 2) & S_1^{(p)}(2) & \dots & 0 \\ S_3^{(p)}(1, 2, 3) & S_2^{(p)}(2, 3) & \dots & 0 \\ \vdots & \vdots & \ddots & \vdots \\ S_n^{(p)}(1, \dots, n) & S_{n-1}^{(p)}(2, \dots, n) & \dots & S_2^{(p)}(n-1, n) \end{vmatrix} \quad (21)$$

is a position-dependent determinant associated with phase p .

Central to this paper is the two-point tensor parameter $\mathbf{A}_2^{(p)}$, which we note generally does not vanish for statistically anisotropic media, since the two-point function $S_2^{(p)}(\mathbf{r})$ depends on the distance $r = |\mathbf{r}|$ as well as the orientation of the vector \mathbf{r} . Second, it is the only tensor parameter in expansion (15) that is independent of the phase p , and hence we define

$$\mathbf{A} \equiv \mathbf{A}_2^{(1)} = \mathbf{A}_2^{(2)} \quad (22)$$

Third, we observe that for macroscopically isotropic media,

$$\mathbf{A} = \mathbf{0}, \quad (23)$$

since \mathbf{A} is traceless, i.e., $\text{Tr}\mathbf{A} = 0$. It is noteworthy that the two-point tensor \mathbf{A} also arises in strong-contrast expansions for the effective stiffness tensor [43].

3.3. Rigorous Bounds and Optimality

Rigorous bounds on the effective conductivity tensor that incorporate up to n -point correlation functions are referred to as n -point bounds [1]. The following are two-point anisotropic generalizations of the Hashin-Shtrikman bounds on σ_e when $\sigma_2 \geq \sigma_1$:

$$\sigma_L^{(2)} \leq \sigma_e \leq \sigma_U^{(2)}, \quad (24)$$

where

$$\sigma_L^{(2)} = \langle \sigma \rangle + (\sigma_2 - \sigma_1)^2 \mathbf{a}_2 \cdot \left[\sigma_1 \mathbf{I} + \frac{(\sigma_1 - \sigma_2)}{\phi_2} \mathbf{a}_2 \right]^{-1}, \quad (25)$$

$$\sigma_U^{(2)} = \langle \sigma \rangle + (\sigma_2 - \sigma_1)^2 \mathbf{a}_2 \cdot \left[\sigma_2 \mathbf{I} + \frac{(\sigma_2 - \sigma_1)}{\phi_1} \mathbf{a}_2 \right]^{-1}, \quad (26)$$

and

$$\mathbf{a}_2 = \frac{1}{d} [\mathbf{A} - \phi_1 \phi_2 \mathbf{I}] \quad (27)$$

is a two-point tensor parameter, which arises in the so-called “weak-contrast” expansion for σ_e [42] and is seen to be trivially related to \mathbf{A} and hence obeys the trace condition

$$\text{Tr } \mathbf{a}_2 = -\phi_1\phi_2. \quad (28)$$

These two-point upper and lower bounds have been derived by a variety of methods. Willis [44] first derived them for $d = 3$ using the anisotropic generalizations of the Hashin–Shtrikman principles. Sen and Torquato [42] obtained them in arbitrary dimension d using the method of Padé approximants [45]. Importantly, the bounds (25) and (26) are achieved by certain oriented singly-coated space-filling ellipsoidal assemblages [46–48] (see Fig. 2) as well as finite-rank laminates [48]. Hence, these bounds are optimal given the phase volume fraction and the two-point information contained in \mathbf{a}_2 . For all optimal structures, one of the phases is generally a disconnected, dispersed phase in a connected matrix phase, except in the trivial instance in which the dispersed phase fills all of space. These two-point bounds are exact to second order in the phase conductivity difference, i.e., for $p \neq q$, we have

$$\sigma_e = \sigma_q \mathbf{I} + \phi_p (\sigma_p - \sigma_q) \mathbf{I} + \frac{(\sigma_p - \sigma_q)^2}{\sigma_q} \mathbf{a}_2 + \mathcal{O}\left(\left[\frac{\sigma_p - \sigma_q}{\sigma_q}\right]^3\right). \quad (29)$$

For statistically anisotropic microstructures in which $S_2^{(p)}(\mathbf{r})$ possesses ellipsoidal symmetry (e.g., oriented similar ellipsoidal inclusions in a matrix with nematic-liquid-crystal structure), the aforementioned two-point parameters are given by

$$\mathbf{A} = (\mathbf{I} - d\mathbf{A}^*)\phi_1\phi_2, \quad \mathbf{a}_2 = -\phi_1\phi_2\mathbf{A}^*, \quad (30)$$

where \mathbf{A}^* is the symmetric *depolarization* tensor of a d -dimensional ellipsoid, which in the principal axes frame has diagonal components or eigenvalues (denoted by A_i^* , $i = 1, \dots, d$, no summation implied) given by the elliptic integrals

$$A_i^* = \left(\prod_{j=1}^d \frac{a_j}{2}\right) \int_0^\infty \frac{dt}{(t + a_i^2) \sqrt{\prod_{j=1}^d (t + a_j^2)}}, \quad i = 1, \dots, d, \quad (31)$$

where a_i is the semiaxis of the ellipsoid along the x_i direction. The depolarization tensor has the property that its trace is unity, i.e.,

$$\text{Tr } \mathbf{A}^* = 1. \quad (32)$$

In the 2D case (ellipse) of aspect ratio $\alpha = a_2/a_1$, (31) can be simplified to yield the exact relation

$$\mathbf{A}^* = \begin{bmatrix} \frac{\alpha}{1+\alpha} & 0 \\ 0 & \frac{1}{1+\alpha} \end{bmatrix}. \quad (33)$$

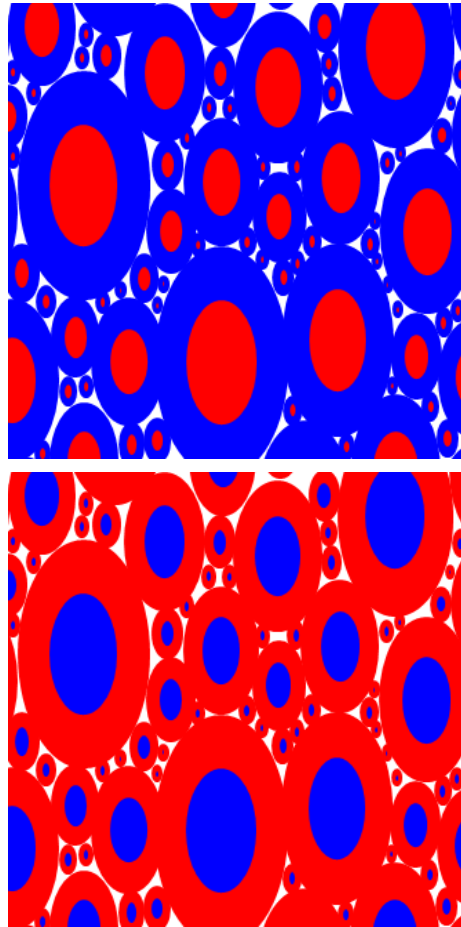


Figure 2. Coated-ellipsoid assemblages consisting of *oriented* composite ellipsoids that are composed of a ellipsoidal core of one phase that is surrounded by a concentric ellipsoidal shell of the other phase such that the fraction of space occupied by the core phase is equal to its overall phase volume fraction [46–48]. The aspect ratio of the composite ellipsoid is set by the eigenvalues of the two-point tensor \mathbf{a}_2 . The composite ellipsoids fill all space, implying that there is a distribution in their sizes ranging to the infinitesimally small. Assuming that the red region constitutes the more conducting phase and the blue region constitutes the less conducting phase, the top and bottom panels show the microstructures that are exactly achieved by the lower bound (25) and upper bound (26), respectively.

From these results, we see that for circles ($\alpha = 1$)

$$A_{11}^* = A_{22}^* = \frac{1}{2}, \quad (\text{circles}) \quad (34)$$

for needle-shaped inclusions aligned along the x_2 -axes ($\alpha = \infty$) and x_1 -axes ($\alpha = 0$), respectively, we have

$$A_{11}^* = 1, \quad A_{22}^* = 0, \quad (\text{needles along the } x_2\text{-axes}) \quad (35)$$

and

$$A_{11}^* = 0, \quad A_{22}^* = 1, \quad (\text{needles along the } x_1\text{-axes}). \quad (36)$$

It is noteworthy, but not surprising in light of the aforementioned results, that the lower bound (25) is exact for a dilute concentration of oriented ellipsoids ($\phi_2 \ll 1$) in a matrix of phase 1, i.e.,

$$\boldsymbol{\sigma}_e = \sigma_1 \mathbf{I} + (\sigma_2 - \sigma_1) \mathbf{I} \cdot \left[\mathbf{I} + \frac{(\sigma_2 - \sigma_1)}{\sigma_1} \mathbf{A}^* \right]^{-1} \phi_2 + \mathcal{O}(\phi_2^2). \quad (37)$$

This relation applies for any size distribution of the ellipsoids, i.e., it is not limited to identical ellipsoids.

Whenever the two-phase system is macroscopically isotropic, i.e., $\boldsymbol{\sigma}_e = \sigma_e \mathbf{I}$ and $\mathbf{a}_2 = -\phi_1 \phi_2 \mathbf{I}/d$, where σ_e is a scalar quantity, the two-point anisotropic bounds (25) and (26) reduce to the d -dimensional Hashin–Shtrikman bounds on σ_e for two-phase isotropic media with $\sigma_2 \geq \sigma_1$:

$$\sigma_L^{(2)} \leq \sigma_e \leq \sigma_U^{(2)}, \quad (38)$$

where

$$\sigma_L^{(2)} = \langle \sigma \rangle - \frac{\phi_1 \phi_2 (\sigma_2 - \sigma_1)^2}{d\sigma_1 + (\sigma_2 - \sigma_1)\phi_1}, \quad (39)$$

$$\sigma_U^{(2)} = \langle \sigma \rangle - \frac{\phi_1 \phi_2 (\sigma_2 - \sigma_1)^2}{d\sigma_2 + (\sigma_1 - \sigma_2)\phi_2}. \quad (40)$$

The Hashin–Shtrikman bounds are realized by the singly coated d -dimensional sphere assemblages [1, 41], second-rank laminates [1, 41], and single-scale Vigdergauz constructions [49, 50]. Accordingly, because the bounds are attainable by certain microstructures, they are the best possible bounds on the effective conductivity of macroscopically isotropic two-phase composites given volume-fraction information only.

3.4. Cross-Property Conductivity-Elastic Moduli Bounds

For macroscopically isotropic two-phase media, Gibiansky and Torquato [51, 52] derived rigorous cross-property bounds that relate the effective elastic moduli to the effective conductivity. In the special case of two-phase media consisting of pores or cracks of arbitrary shape and size distributed throughout a solid material, these formulas simplify considerably [51, 52]. Let the bulk modulus, shear modulus and Young's modulus of the solid phase be denoted by K , G and E , respectively. Denote by K_e , G_e and E_e the effective bulk modulus, shear modulus and Young's modulus, respectively. Note that for macroscopically isotropic structure, there are only two independent elastic moduli. For example, given K_e and G_e of a structure, any other quantities such as E_e can be derived. The general cross-property bounds that rigorously link the effective elastic moduli to the effective conductivity in 2D are given by

$$\frac{K}{K_e} - 1 \geq \frac{K + G}{2G} \left[\frac{\sigma}{\sigma_e} - 1 \right], \quad (41)$$

$$\frac{G}{G_e} - 1 \geq \frac{K + G}{K} \left[\frac{\sigma}{\sigma_e} - 1 \right], \quad (42)$$

$$\frac{E}{E_e} - 1 \geq \frac{3}{2} \left[\frac{\sigma}{\sigma_e} - 1 \right]. \quad (43)$$

In the low-density asymptotic limit, i.e., $\phi \ll 1$, one can assume that $\sigma_e/\sigma \ll 1$, $K_e/K \ll 1$, $G_e/G \ll 1$, and $E_e/E \ll 1$. Under such conditions, the cross-property bounds (41)-(43) reduce to

$$\frac{K_e}{K} \leq \frac{2G}{K + G} \frac{\sigma_e}{\sigma} = (1 - \nu) \frac{\sigma_e}{\sigma}, \quad (44)$$

$$\frac{G_e}{G} \leq \frac{K}{K + G} \frac{\sigma_e}{\sigma} = \frac{(1 + \nu)}{2} \frac{\sigma_e}{\sigma}, \quad (45)$$

and

$$\frac{E_e}{E} \leq \frac{2}{3} \frac{\sigma_e}{\sigma}, \quad (46)$$

respectively. Here ν is the Poisson's ratio and in 2D is bounded according to

$$-1 \leq \nu \leq 1. \quad (47)$$

Equations (41) - (46) only apply to statistically isotropic structures or statistically anisotropic structures with 3- or 6-fold rotational symmetry. Note that measurement of the elastic moduli in conjunction with the cross-property bounds (41) - (46) allows one to obtain a *lower bound* on the effective conductivity. Similarly, conductivity information and bounds (41) - (46) enables one to bound the elastic moduli from above. However, effective shear modulus G_e and effective Young's modulus E_e of certain networks, such as honeycomb-like (e.g., Voronoi and Delaunay-centroidal networks) and square-like ones, are far from optimal, i.e., far from the corresponding upper bounds (42), (43), (46), and (47) due to the bending modes of the structures [18, 19, 53]. Subsequently, we will only employ the upper bounds to estimate G_e and E_e for the triangular networks.

4. Application to Low-Density Network Solids

Of particular interest in this paper are applications of the two-point anisotropic bounds (25) and (26) to low-density networks. Assuming that phase 2 is the low-density, more conducting phase (i.e., $\phi_2 \ll 1$ and $\sigma_2 \geq \sigma_1$), these bounds become

$$\boldsymbol{\sigma}_e \geq \sigma_1 \mathbf{I} + (\sigma_2 - \sigma_1) \mathbf{I} \cdot \left[\mathbf{I} - \frac{(\sigma_1 - \sigma_2)}{\sigma_1} \mathbf{A}^* \right]^{-1} \phi_2 \quad (48)$$

$$\boldsymbol{\sigma}_e \leq \sigma_1 \mathbf{I} + (\sigma_2 - \sigma_1) \left[\mathbf{I} - \frac{(\sigma_2 - \sigma_1)}{\sigma_2} \mathbf{A}^* \right] \phi_2 \quad (49)$$

where \mathbf{A}^* is defined in Eq. (31).

Importantly, we will see that there are anisotropic network structures in two and three dimensions that attain the upper bound (26) and hence are optimal. Elsewhere it was shown that macroscopically isotropic 2D ordered networks with 4-fold rotational symmetry (e.g., square tessellation) and 6-fold rotational symmetry (e.g., honeycomb and equilateral-triangular tessellations) attain the upper bound and hence are optimal [53]. In these instances, $\mathbf{A}^* = \phi_1\phi_2/2$, and the upper bound reduces to the corresponding Hashin-Shtrikman upper bound, as obtained from (40).

In the extreme case in which $\sigma_1 = 0$, upper bound (26) reduces to the following simple form:

$$\sigma_e \leq \sigma_U^{(2)} = \frac{1}{2} \left(1 + \frac{\mathbf{A}}{\phi}\right) \phi \sigma \quad (50)$$

Henceforth when referring to the properties of the solid phase, we drop the subscripts so that $\phi \equiv \phi_2$ and $\sigma \equiv \sigma_2$. Note that the lower bound (49) is trivially zero because it corresponds to a microstructure in which the perfectly insulating phase 1 is connected (see Fig. 2). For macroscopically isotropic media, the two-point tensor coefficient \mathbf{A} vanishes, as stated in Eq. (23), and the upper bound (50) reduces to the Hashin-Shtrikman bound $\sigma_U^{(2)}$ on the scalar effective conductivity σ_e :

$$\sigma_U^{(2)} = \frac{1}{2} \phi \sigma. \quad (51)$$

In the subsequent sections, we will focus on this extreme case.

5. Network Analysis

In this section, we develop a general scheme to compute the effective conductivity tensor σ_e of 2D ordered and disordered cellular network structures in which one phase consists of connected infinitesimally thin channels (henceforth called the “channel” phase) and the other is a disconnected and insulating “void” phase. We also exactly evaluate the two-point tensor \mathbf{A} , defined by (22), for a certain class of such networks.

5.1. Effective Conductivity Tensor

Here we denote the conductivity and volume fraction of the “channel” phase by σ and ϕ , respectively. To determine the effective conductivity σ_e , we consider the conduction problem in a fundamental cell (i.e., smallest periodic repeat unit). For our purposes, we consider rectangular fundamental cells. We set the potentials (or temperatures) at the two opposing boundaries in the x_i direction to be T_A and T_B , and the applied field \mathbf{E}_0 , which is equal to $\langle E_i \rangle$ (the average of local field in the x_i direction), is given by

$$E_0 = \langle E_i \rangle = -\frac{T_B - T_A}{L_i}, \quad (52)$$

where $E_0 = |\mathbf{E}_0|$, and L_i is the side length of the fundamental cell in the x_i direction. In the orthogonal direction, we apply periodic boundary conditions. We denote the magnitude of the flux by $J \equiv |\mathbf{J}|$. For example, if we consider the conduction problem in the x_1 direction, the boundary conditions are given by

$$\left. \begin{aligned} T(x_1, x_2 + L_2) &= T(x_1, x_2) \\ T(x_1 + L_1, x_2) &= T(x_1, x_2) - E_0 L_1 \end{aligned} \right\} \quad (53)$$

As a general guideline, when considering an applied field in one of the orthogonal directions, it is convenient to choose the fundamental cell so that it possesses reflection symmetry with respect to this direction, if possible.

Figure 3 schematically shows the general setup for the conduction problem in a fundamental cell, which, for purposes of illustration, show an applied field \mathbf{E}_0 in the x_1 -direction. The lengths of the fundamental cell in the x_1 - and x_2 -directions are denoted by L_1 and L_2 , respectively.

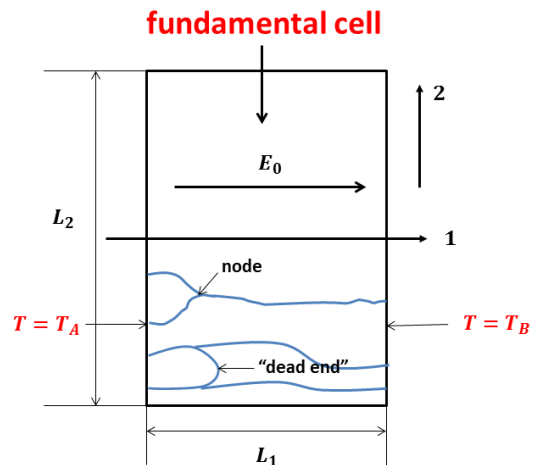


Figure 3. A general framework of the conduction problem in a fundamental cell (which in this case is in the x_1 direction). The lengths of the fundamental cell in the x_1 and x_2 directions are denoted by L_1 and L_2 , respectively. The potentials (or temperatures) at the two opposing boundaries in the x_1 direction are set to be T_A and T_B , and the corresponding applied field in the x_1 direction is denoted by E_0 .

The effective conductivity tensor is determined by the averaged Ohm’s (Fourier’s) law given by relation (14). Since our coordinate system is aligned with the principal axes frame, then we need only consider the diagonal components of the effective conductivity tensor. We denote by $(\sigma_e)_{II}$ the II -component of the effective conductivity tensor (no summation implied).

Thus, according to Eqs. (14) and (52), we have

$$\langle J_i \rangle = (\sigma_e)_{II} \langle E_i \rangle = -(\sigma_e)_{II} \frac{T_B - T_A}{L_i}. \quad (54)$$

where

$$\langle \mathbf{J} \rangle = \frac{1}{\Omega} \int \mathbf{J}(\mathbf{x}) dV = \frac{1}{\Omega} \int \mathbf{J}(\mathbf{x}) dV_2, \quad (55)$$

$\Omega = L_1 L_2$ is the volume of the fundamental cell, and $\int dV_2$ denotes the integral over the space occupied by the channel phase. Applying Eq. (11) along the conduction path between opposing boundaries in the x_i -direction, we get

$$\int_A^B J dl = -\sigma(T_B - T_A), \quad (56)$$

The path integral Eq. (56) is the same for any path connecting the two opposing boundaries, which should not contain “dead ends”, defined to be channels that are not topologically connected to boundaries or channels with zero flux that are not perpendicular to the applied field. From Eqs. (54) and (56), we get

$$(\sigma_e)_{II} E_0 = \frac{(\sigma_e)_{II} \int_A^B J dl}{\sigma L_i} = \langle J_i \rangle, \quad (57)$$

Therefore, $(\sigma_e)_{II}$ is

$$\frac{(\sigma_e)_{II}}{\sigma} = \frac{\langle J_i \rangle L_i}{\int_A^B J dl}. \quad (58)$$

Note that in the limit $\phi \rightarrow 0$ (i.e., the thickness of the channels goes to 0), the magnitude of flux J is piecewise constant for such cellular network structures. Furthermore, for structures consisting of piecewise straight channels, the flux \mathbf{J} is piecewise constant. For any cellular network, letting $J_{m,n}$ represent the (signed) flux flowing from node m to n (where the concept of a node schematically shown in Figure 2), Ohm’s and Kirchhoff’s laws can be written in a discrete form,

$$J_{m,n} = \sigma(T_m - T_n) H_{m,n}, \quad (59)$$

and similarly, the divergence-free condition (12) can be written as

$$\sum_n J_{m,n} = 0 \quad \forall m. \quad (60)$$

Here $H_{m,n}$ is the generalized adjacency matrix of the graph formed by the cellular network. $H_{m,n}$ takes the value $1.0/a_{m,n}$, where $a_{m,n}$ is the length of the channel connecting nodes m and n if there exists such a channel, and 0 otherwise. By solving Eqs. (59) and (60) and taking into account the symmetry of the cellular network structure, we obtain the magnitude of the flux in each channel within the fundamental

cell, which is then used to compute $\langle J_i \rangle$ and $\int_A^B J dl$. Finally, the II -component of the effective conductivity $(\sigma_e)_{II}$ tensor is determined from Eq. (58).

To quantify how much the effective conductivity σ_e of a certain structure deviates from the upper bound $\sigma_U^{(2)}$, or how “tortuous” the conduction path is, we introduce what we call the “tortuosity” tensor \S τ :

$$\tau = \begin{bmatrix} \tau_1 & 0 \\ 0 & \tau_2 \end{bmatrix} \quad (61)$$

Here $\tau_I (I = 1, 2)$ denotes the I -th eigenvalue of τ and is given by

$$\tau_I = (\sigma_U^{(2)})_{II} / (\sigma_e)_{II}, \quad (62)$$

where $(\sigma_U^{(2)})_{II}$ and $(\sigma_e)_{II}$ are the I -th eigenvalues of $\sigma_U^{(2)}$ and σ_e , respectively. For macroscopically isotropic structures, the tortuosity reduces to a scalar quantity τ . Note that for optimal structures, the eigenvalues $\tau_1 = \tau_2 = 1$.

Using these procedures, we first determine the effective conductivities of ordered (periodic) hyperuniform networks shown in Fig. 4, which include both macroscopically isotropic and anisotropic varieties. The computed effective conductivity and tortuosity tensors of these structures are listed in Table 1. Note that among all of the macroscopically isotropic structures investigated, the honeycomb network [Fig. 4(a)], triangular network [Fig. 4(b)], kagomé network [Fig. 4(c)], and square network [a special case of the rectangular and rhombic networks in Fig. 4 (h) and (i)] possess the optimal value of the effective conductivity, i.e., they achieve the upper bound (51) [55]. The structures shown in Fig. 4 (d), (e), (f), and (g), on the other hand, possess suboptimal effective conductivities. Note that the network consisting of touching circles shown in Fig. 4 (g) possesses “dead ends”, a structural feature that leads to a suboptimal effective conductivity. Indeed, this network possesses the lowest effective conductivity σ_e , or the highest scalar tortuosity τ , among all of the networks investigated in this study.

5.2. Effective Conductivity of Intersecting Parallel-Channel Cellular Structures

We now consider cellular structures that are constructed by superposing $N (N \geq 2)$ sets of intersecting

\S Traditionally tortuosity has been defined to be a purely geometric scalar quantity: the ratio of the average length of the fluid paths and the geometrical length of the sample [54]. Our new tortuosity tensor is distinguished from earlier definition in that it is based on the transport behavior (not purely geometrical features) and anisotropic media.

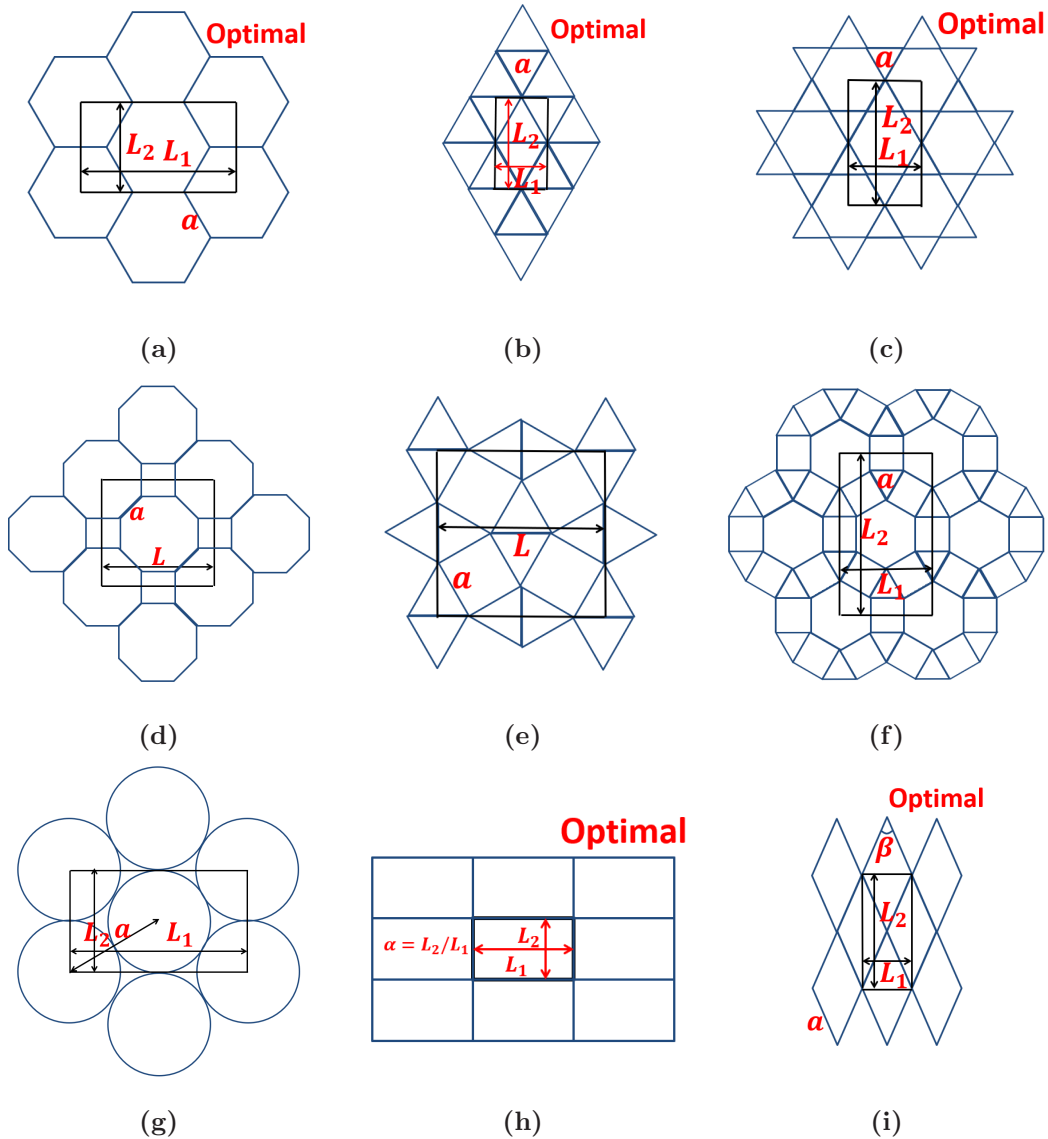


Figure 4. Illustrations of various periodic cellular network structures and their fundamental cells. The fundamental cells are indicated in black. The lengths of the fundamental cell in the x_1 and x_2 directions are denoted by L_1 and L_2 , respectively. In certain cases where $L_1 = L_2$, we simply use L to denote both lengths. (a) Honeycomb network. (b) Triangular network. (c) Kagomé network. (d) Octagonal network. (e) Snub square network. (f) Overlapping dodecagonal network. (g) Triangular lattice of circles. (h) Rectangular network. Note that square network is a special case of rectangular network, where the aspect ratio $\alpha = 1$. (i) Rhombic network. Note that square network is a special case of rhombic network, where $L_1 = L_2$ and $\beta = \pi/2$.

parallel channels oriented in directions with polar angles $\psi_1, \psi_2, \dots, \psi_N$, respectively, as schematically shown in Fig. 5. We stress that the parallel channels in each set are not required to be equally spaced, and thus the networks discussed here include disordered ones [see Fig. 5(b) for an example]. Note that the rectangular and rhombic networks shown in Figs. 4 (h) and (i) are special examples of this type of structures. The relative volume fraction of the i -th set of channels is

denoted by c_i ($i = 1, 2, \dots, N$, and $\sum_{i=1}^N c_i = 1$), where $c_i = \phi_{2,i}/\phi$ and $\phi_{2,i}$ is the volume fraction of the i -th set of channels.

For such an intersecting parallel-channel network, we can compute the effective conductivity σ_e exactly. Specifically, application of the procedure described in Sec. 5.1 to such a general structure yields the following

Table 1. Effective conductivity tensor σ_e and tortuosity tensor τ of various periodic network structures as shown in Fig. 4. Note that the honeycomb, triangular, kagomé, square, rectangular and rhombic networks possess the optimal values of the effective conductivity.

Network	$\sigma_e/(\phi_2\sigma)$	τ
Honeycomb	$\begin{bmatrix} \frac{1}{2} & 0 \\ 0 & \frac{1}{2} \end{bmatrix}$	$\begin{bmatrix} 1 & 0 \\ 0 & 1 \end{bmatrix}$
Triangular	$\begin{bmatrix} \frac{1}{2} & 0 \\ 0 & \frac{1}{2} \end{bmatrix}$	$\begin{bmatrix} 1 & 0 \\ 0 & 1 \end{bmatrix}$
Kagomé	$\begin{bmatrix} \frac{1}{2} & 0 \\ 0 & \frac{1}{2} \end{bmatrix}$	$\begin{bmatrix} 1 & 0 \\ 0 & 1 \end{bmatrix}$
Octagonal	$\begin{bmatrix} \frac{3+2\sqrt{2}}{12} & 0 \\ 0 & \frac{3+2\sqrt{2}}{12} \end{bmatrix}$	$\begin{bmatrix} 1.0294 & 0 \\ 0 & 1.0294 \end{bmatrix}$
Snub square	$\begin{bmatrix} \frac{4+2\sqrt{3}}{15} & 0 \\ 0 & \frac{4+2\sqrt{3}}{15} \end{bmatrix}$	$\begin{bmatrix} 1.0048 & 0 \\ 0 & 1.0048 \end{bmatrix}$
Overlapping dodecagonal	$\begin{bmatrix} \frac{2+\sqrt{3}}{8} & 0 \\ 0 & \frac{2+\sqrt{3}}{8} \end{bmatrix}$	$\begin{bmatrix} 1.0718 & 0 \\ 0 & 1.0718 \end{bmatrix}$
Triangular lattice of circles	$\begin{bmatrix} \frac{9}{2\pi^2} & 0 \\ 0 & \frac{9}{2\pi^2} \end{bmatrix}$	$\begin{bmatrix} 1.0966 & 0 \\ 0 & 1.0966 \end{bmatrix}$
Rectangular	$\begin{bmatrix} \frac{1}{1+\alpha} & 0 \\ 0 & \frac{\alpha}{1+\alpha} \end{bmatrix}$	$\begin{bmatrix} 1 & 0 \\ 0 & 1 \end{bmatrix}$
Rhombic	$\begin{bmatrix} \sin^2(\frac{\beta}{2}) & 0 \\ 0 & \cos^2(\frac{\beta}{2}) \end{bmatrix}$	$\begin{bmatrix} 1 & 0 \\ 0 & 1 \end{bmatrix}$

effective conductivity σ_e :

$$\sigma_e = \begin{bmatrix} \sum_{i=1}^N \cos^2(\psi_i)c_i & \sum_{i=1}^N \cos(\psi_i)\sin(\psi_i)c_i \\ \sum_{i=1}^N \cos(\psi_i)\sin(\psi_i)c_i & \sum_{i=1}^N \sin^2(\psi_i)c_i \end{bmatrix} \phi. \quad (63)$$

5.3. Demonstration of Optimality for Intersecting Parallel-Channel Cellular Structures

We now prove that the effective conductivity tensor (63) for any intersecting parallel-channel network is optimal by showing that it corresponds to the the upper bound $\sigma_U^{(2)}$ on σ_e . We begin by computing the

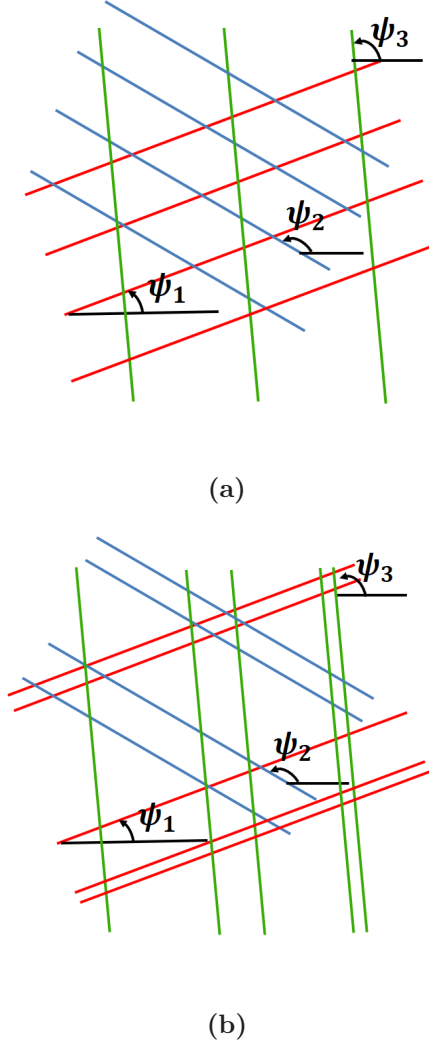


Figure 5. Schematics of ordered (a) and disordered (b) cellular structures consisting of three sets of intersecting parallel channels oriented in directions with polar angles ψ_1, ψ_2 and ψ_3 , respectively. We stress that the parallel channels in each set are not required to be equally spaced, and thus the networks discussed here include disordered varieties.

two-point tensor coefficient \mathbf{A} of such a network, which is explicitly given by

$$\mathbf{A} = \frac{1}{\pi} \lim_{\delta \rightarrow 0} \int_{\delta}^{\infty} \frac{dr}{r} \int_0^{2\pi} d\theta \chi(r, \theta) \begin{bmatrix} \cos(2\theta) & \sin(2\theta) \\ \sin(2\theta) & -\cos(2\theta) \end{bmatrix} \quad (64)$$

where $\chi(r, \theta) = S_2(r, \theta) - \phi^2$ is the autocovariance function of the cellular network, and $S_2(r, \theta)$ is the two-point correlation function of the channel phase. The autocovariance function $\chi(r, \theta)$ can be decomposed into

two parts:

$$\chi(r, \theta) = \sum_{i=1}^N [S_{2,ii}(r, \theta) - \phi_{2,i}^2] + \sum_{i < j} [S_{2,ij}(r, \theta) - 2\phi_{2,i}\phi_{2,j}], \quad (65)$$

where the first part corresponds to the two-point correlation between channels in the same set, and the second part corresponds to the two-point cross-correlation between channels in different sets, and $\phi_{2,i}$ is the volume fraction the i -th set of channels. Since the two-point cross-correlation term $S_{2,ij}(r, \theta) - 2\phi_{2,i}\phi_{2,j}$ depends only on the distance r , i.e., independent of the orientation θ , the contribution to \mathbf{A} from the second part is $\mathbf{0}$. By adding up the contributions to \mathbf{A} from the self-correlation of each individual set of intersecting parallel channels, we find

$$\mathbf{A} = \begin{bmatrix} \sum_{i=1}^N \cos(2\psi_i) c_i & \sum_{i=1}^N \sin(2\psi_i) c_i \\ \sum_{i=1}^N \sin(2\psi_i) c_i & -\sum_{i=1}^N \cos(2\psi_i) c_i \end{bmatrix} \phi. \quad (66)$$

We can diagonalize the above matrix to obtain the eigenvalues for \mathbf{A} once the relative volume fractions and orientations of each set of intersecting parallel channels are given. In general, the “superposition” of sets of intersecting parallel channels produces a macroscopically anisotropic structure, and the corresponding \mathbf{A} is not $\mathbf{0}$.

By substituting \mathbf{A} , given by Eq. (66), into Eq. (50), we see that the upper bound $\sigma_U^{(2)}$ for these structures is exactly the same as σ_e given by Eq. (63). Thus, we have rigorously demonstrated that anisotropic structures consisting of sets of intersecting parallel channels achieve the two-point anisotropic generalizations of the Hashin–Shtrikman bound (26) on σ_e , regardless of whether they are ordered or disordered, hyperuniform or nonhyperuniform.

In addition, we note that in certain special cases, where the N sets of intersecting parallel channels have identical relative volume fraction, i.e., $c_i = \frac{1}{N}$ ($i = 1, 2, \dots, N$), and the channels are superpositioned in a way such that the overall structure possesses N -fold rotational symmetry, we can show that $\mathbf{A} = \mathbf{0}$. Specifically, without loss of generality, we can have one set of channels aligned with the horizontal axis, and the other sets oriented in directions with polar angles $\psi = \frac{\pi}{N}, \dots, \frac{\pi(N-1)}{N}$, respectively, with \mathbf{A} now given by

$$\mathbf{A} = \begin{bmatrix} \sum_{i=0}^{N-1} \cos(\frac{2\pi}{N}i) & \sum_{i=0}^{N-1} \sin(\frac{2\pi}{N}i) \\ \sum_{i=0}^{N-1} \sin(\frac{2\pi}{N}i) & -\sum_{i=0}^{N-1} \cos(\frac{2\pi}{N}i) \end{bmatrix} \frac{\phi}{N} = \mathbf{0}. \quad (67)$$

Thus, the resulting structure is macroscopically isotropic.

5.4. Cross-Property Relations

For periodic cellular structures with 3-, 4- or 6-fold rotational symmetry, the cross-property bound (44) allows us to obtain upper bounds on the effective bulk moduli given the measurement of the effective conductivity of the structures. Interestingly, whenever the effective conductivity σ_e of certain structure is optimal, so are the effective bulk moduli. The results are summarized in Table 2. Note that the square, honeycomb, and kagomé networks possess optimal effective bulk moduli, i.e., they achieve the upper bound (44).

Table 2. Upper bounds on the effective moduli K_e of certain periodic network structures in Fig. 4, which are scaled by modulus K , and volume fraction ϕ of the “channel” phase. It is noteworthy that the square, honeycomb and kagomé networks possess optimal K_e .

Network	$K_e/(K\phi)$
Honeycomb	$0.5(1 - \nu)$
Triangular	$0.5(1 - \nu)$
Kagomé	$0.5(1 - \nu)$
Square	$0.5(1 - \nu)$
Octagonal	$\frac{3+2\sqrt{2}}{12}(1 - \nu)$
Snub square	$\frac{4+2\sqrt{3}}{15}(1 - \nu)$
Overlapping dodecagonal	$\frac{2+\sqrt{3}}{8}(1 - \nu)$
Triangular lattice of circles	$\frac{9}{2\pi^2}(1 - \nu)$

5.5. Results for Arbitrary Phase Contrast

It should not go unnoticed that many of the aforementioned results are straightforwardly extended to cases in which the void or matrix phase has non-zero phase properties. In such instances, the lower bounds (48) no longer vanish. Note that whenever the network structure is optimal (i.e., maximizes the effective conductivity), the upper bound (49) on effective

conductivity is an exact result (i.e., achieved by certain structures) for arbitrary phase contrast. For example, in Fig. 6, we plot the effective conductivity for the optimal case of the aforementioned oriented singly-coated space-filling ellipsoidal assemblages shown in Fig. 2 with an aspect ratio $\alpha = 5.0$ as a function of the volume fraction of the more conducting phase ϕ_2 at phase contrast ratios $\sigma_2/\sigma_1 = 2.0, 5.0,$ and 10.0 .

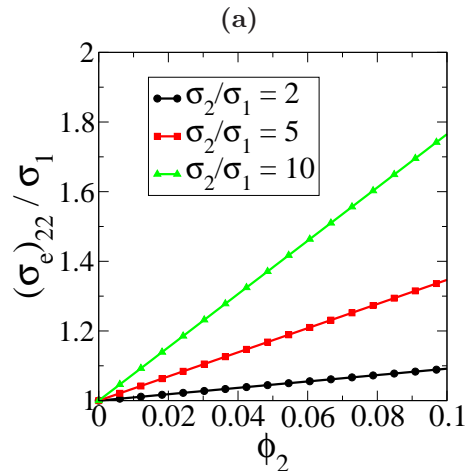
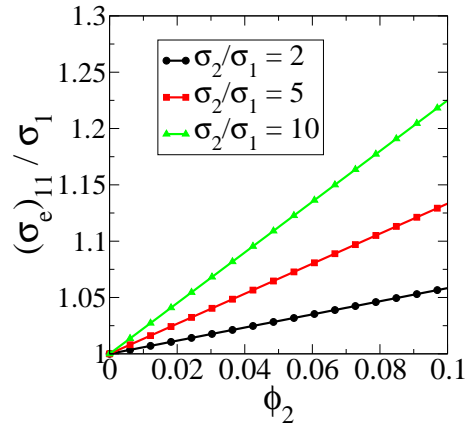


Figure 6. The principal components of the effective conductivity $(\sigma_e)_{11}$ (a) and $(\sigma_e)_{22}$ (b) of oriented singly-coated space-filling ellipsoidal assemblages shown in Fig. 2 with an aspect ratio $\alpha = 5.0$ as a function of the volume fraction of the more conducting phase ϕ_2 at phase contrast ratios $\sigma_2/\sigma_1 = 2.0, 5.0,$ and 10.0 , as computed from Eq. (49). The effective conductivity of this anisotropic structure possesses optimal values.

6. Effective Conductivity and Elastic Moduli of Hyperuniform and Nonhyperuniform Disordered Networks

In this section, we determine the effective conductivity and elastic moduli of various statistically isotropic disordered hyperuniform and nonhyperuniform networks. Our goal is to investigate how hyperuniformity affects the effective conductivity and elastic moduli, and how close these effective properties of disordered hyperuniform networks can come to being optimal.

6.1. Mapping Disordered Point Patterns to Disordered Networks

We map various 2D disordered nonhyperuniform and hyperuniform point patterns into 2D cellular network structures by the three types of tessellations mentioned in Sec. 2.3: Delaunay, Voronoi and Delaunay-centroidal tessellations. We then compute the effective conductivities of the networks. These point patterns include nonhyperuniform and hyperuniform ones in square domains subject to periodic boundary conditions. For nonhyperuniform point patterns, we consider Poisson point patterns (which are uncorrelated on all length scales) and those associated with the centroids of equal-sized hard disks in packings generated by the random-sequential-addition (RSA) process [56] with $N = 100$ points in each pattern. We consider hyperuniform point patterns associated with the centroids of equal-sized hard disks in maximally-random-jammed (MRJ) packings [57] with $N = 100$ points in each pattern, and various disordered stealthy hyperuniform ones with different χ values [38, 39] and $N = 150$ points in each pattern. These stealthy point patterns are generated using the procedure described in Ref. [39]. Specifically, an optimization objective function that targets the structure factor $S(k)$ to be exactly zero for a range of small wavenumbers is employed, which guarantees the stealthiness of the resulting point patterns. As mentioned above, when $0 < \chi < 0.5$, the point pattern is disordered and henceforth we will employ point patterns with χ values in this range. Specifically, we pick three χ values: 0.3, 0.4, and 0.49 [38, 39].

The three types of constructed cellular network structures corresponding to Poisson, RSA and MRJ point patterns that are not stealthy are shown in Fig. 7, while those corresponding to disordered stealthy hyperuniform point patterns are shown in Fig. 8. Note that in those Voronoi and Delaunay-centroidal networks, the underlying point patterns are colored in red, and the conducting “channels” are colored in blue. In those Delaunay networks, the points in the underlying point patterns are just the vertices of the triangles, which are colored in blue. As χ

increases, the fraction of hexagonal cells compared to all other possible polygonal cells in the corresponding networks increases, which is a manifestation of the increasing short-range order of the networks. Indeed, at $\chi = 0.49$, the average fraction of hexagonal, pentagonal, and heptagonal cells for the Voronoi and Delaunay-centroidal networks (averaged over ten configurations) is equal to 96.8%, 1.6% and 1.6%, respectively. Observe that all the cellular network structures considered here are statistically isotropic by construction, and hence their effective conductivity is a scalar, which we denote by σ_e . Moreover, we conjecture that the networks derived from the stealthy hyperuniform point patterns are also stealthy and hyperuniform, which is based on strong numerical evidence from a previous photonic study [29]. However, we note that in a rigorous mathematical sense, this is still an open question, as we discuss in Sec. 7.

6.2. Effective Conductivity

Here we compute the effective conductivity σ_e and tortuosity τ of these disordered statistically isotropic network structures by computationally solving the equation described in Sec. 5.1. For each system, we average over ten configurations. The results are summarized in Table 3.

It is noteworthy that Poisson networks have the lowest effective conductivity due to the complete absence of order on all length scales. On the other hand, for those point patterns associated with hard-disk packings, as the packings approach jamming and the point patterns tend toward hyperuniform states, the effective conductivity of the corresponding network structures increases. Moreover, for those point patterns that are indeed hyperuniform and stealthy, as χ increases, i.e., the short-range order of the corresponding networks dramatically increases [39], the effective conductivity of the corresponding network increases. Interestingly, when $\chi = 0.49$, the corresponding statistically isotropic networks are nearly optimal in terms of their effective conductivity, i.e., achieve the upper bound (51). These observations suggest that for disordered statistically isotropic Voronoi, Delaunay, and “Delaunay-centroidal” cellular network structures to achieve optimal effective conductivity, both short-range and long-range orders are necessary. These networks are ideal for heat dissipation as well as electrical and fluid (see Sec. 7) transport through the channel phase. In addition, among the three types of tessellations investigated here, the Voronoi tessellations generally possess higher effective conductivity than the Delaunay and Delaunay-centroidal tessellations of the same point pattern, except for the Poisson point pattern.

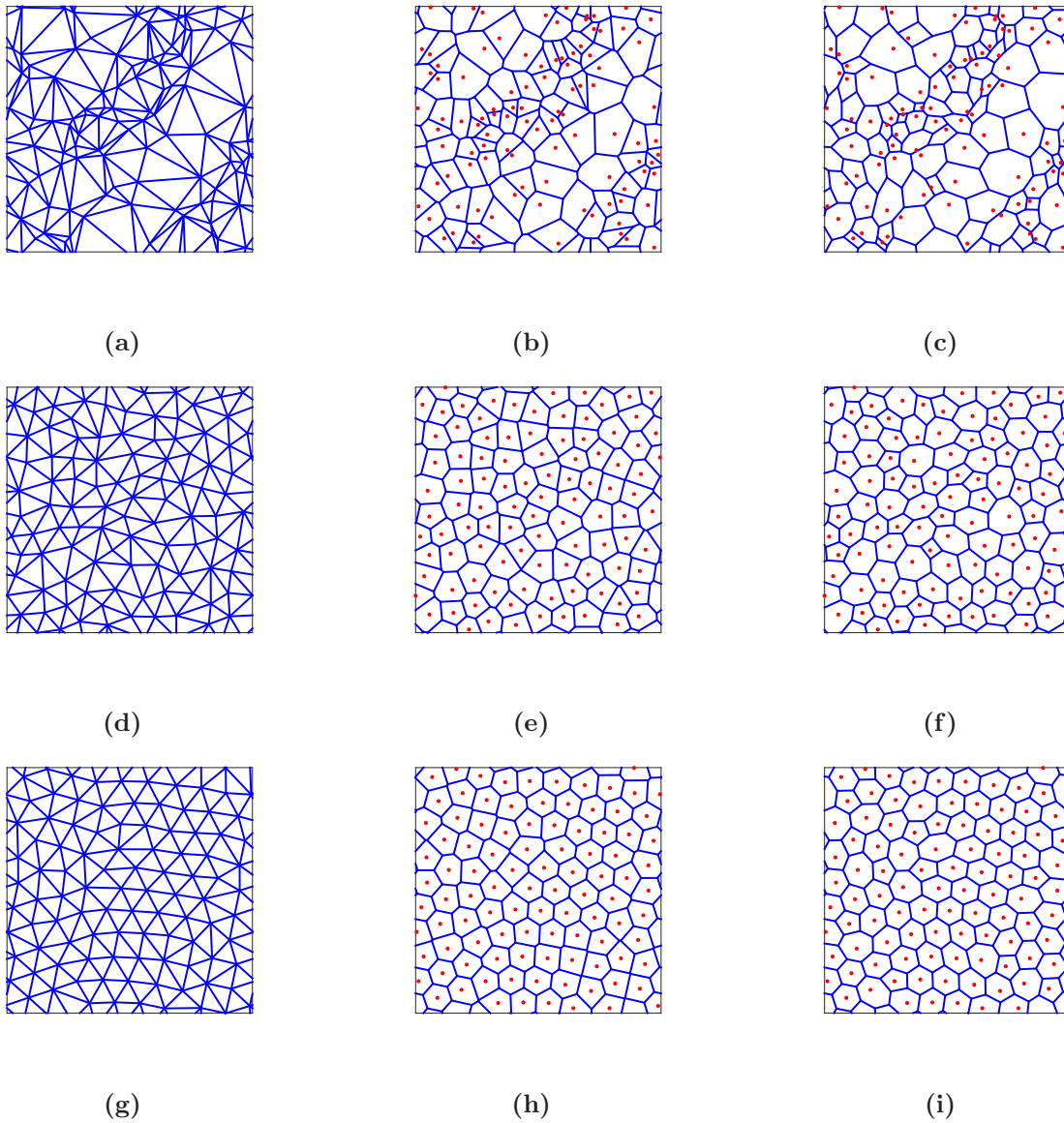


Figure 7. Representative disordered nonstealthy cellular network structures mapped from various point patterns. There are $N = 100$ points in each underlying point pattern. Note that in those Voronoi and Delaunay-centroidal networks, the underlying point patterns are colored in red, and the conducting “channels” are colored in blue. In those Delaunay networks, the points in the underlying point patterns are just the vertices of the triangles, which are colored in blue. (a) Delaunay network of Poisson point pattern. (b) Voronoi network of Poisson point pattern. (c) Delaunay-centroidal network of Poisson point pattern. (d) Delaunay network of RSA point pattern. (e) Voronoi network of RSA point pattern. (f) Delaunay-centroidal network of RSA point pattern. (g) Delaunay network of MRJ point pattern. (h) Voronoi network of MRJ point pattern. (i) Delaunay-centroidal network of MRJ point pattern.

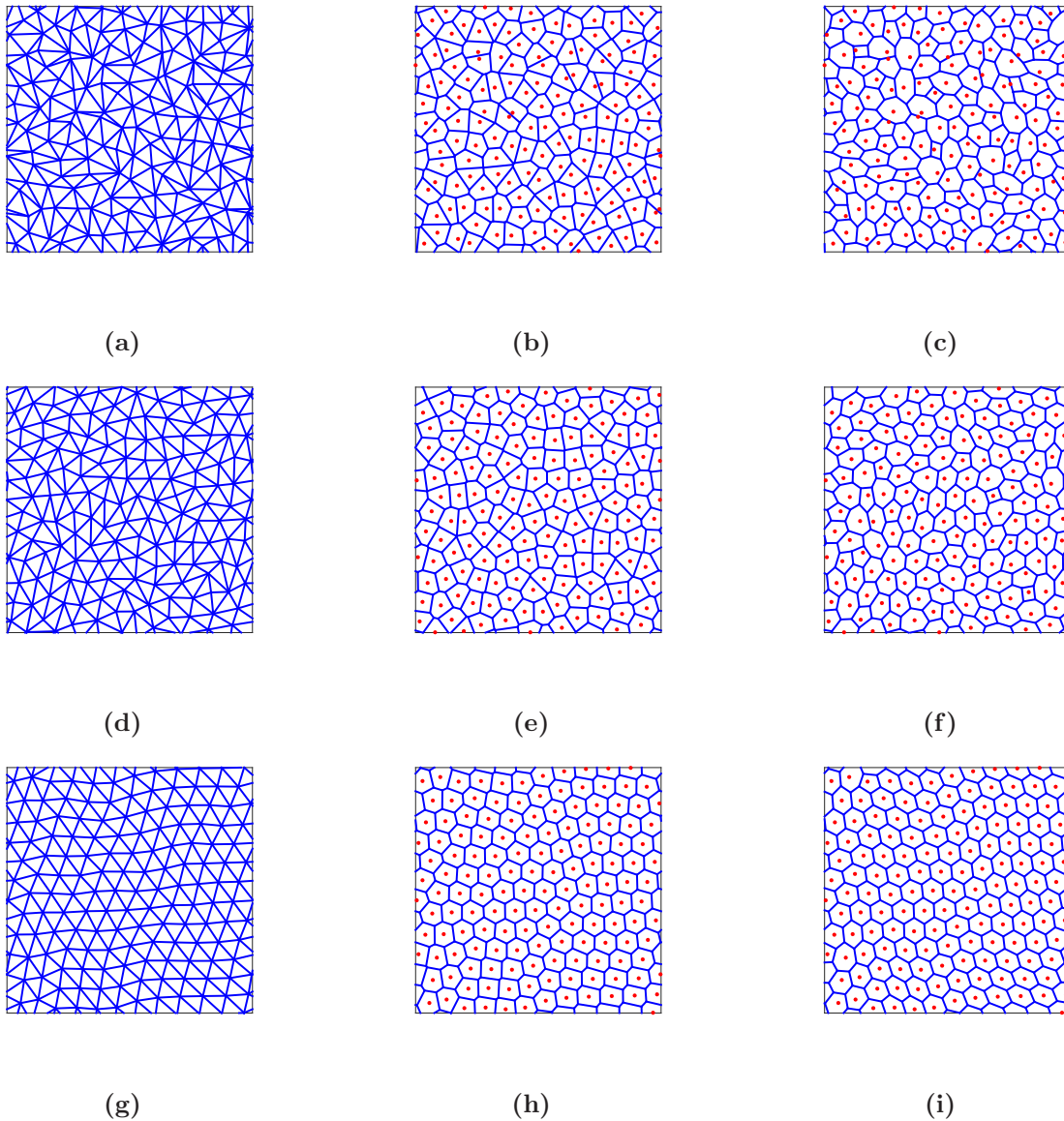


Figure 8. Representative disordered stealthy cellular network structures mapped from various point patterns. There are $N = 150$ points in each underlying point pattern. Note that in those Voronoi and Delaunay-centroidal networks, the underlying point patterns are colored in red, and the conducting “channels” are colored in blue. In those Delaunay networks, the points in the underlying point patterns are just the vertices of the triangles, which are colored in blue. (a) Delaunay network of stealthy point pattern with $\chi = 0.3$. (b) Voronoi network of stealthy point pattern with $\chi = 0.3$. (c) Delaunay-centroidal network of stealthy point pattern with $\chi = 0.3$. (d) Delaunay network of stealthy point pattern with $\chi = 0.4$. (e) Voronoi network of stealthy point pattern with $\chi = 0.4$. (f) Delaunay-centroidal network of stealthy point pattern with $\chi = 0.4$. (g) Delaunay network of stealthy point pattern with $\chi = 0.49$. (h) Voronoi network of stealthy point pattern with $\chi = 0.49$. (i) Delaunay-centroidal network of stealthy point pattern with $\chi = 0.49$.

Table 3. Effective conductivity σ_e (scaled by the conductivity σ and volume fraction ϕ of the conducting “channels”) and tortuosity τ of various isotropic disordered hyperuniform and nonhyperuniform networks. The results are averaged over ten configurations for each system.

Point pattern	Tessellation	$\sigma_e/(\sigma\phi)$	τ
Poisson	Delaunay	0.4643	1.0769
Poisson	Voronoi	0.4473	1.1178
Poisson	Delaunay-centroidal	0.4490	1.1136
RSA	Delaunay	0.4860	1.0288
RSA	Voronoi	0.4907	1.0190
RSA	Delaunay-centroidal	0.4859	1.0290
MRJ	Delaunay	0.4887	1.0231
MRJ	Voronoi	0.4971	1.0058
MRJ	Delaunay-centroidal	0.4890	1.0225
Stealthy with $\chi = 0.3$	Delaunay	0.4698	1.0643
Stealthy with $\chi = 0.3$	Voronoi	0.4842	1.0326
Stealthy with $\chi = 0.3$	Delaunay-centroidal	0.4677	1.0691
Stealthy with $\chi = 0.4$	Delaunay	0.4751	1.0524
Stealthy with $\chi = 0.4$	Voronoi	0.4896	1.0212
Stealthy with $\chi = 0.4$	Delaunay-centroidal	0.4762	1.0500
Stealthy with $\chi = 0.49$	Delaunay	0.4937	1.0128
Stealthy with $\chi = 0.49$	Voronoi	0.4984	1.0032
Stealthy with $\chi = 0.49$	Delaunay-centroidal	0.4952	1.0097

6.3. Cross-Property Relations

The disordered networks investigated here are elastically isotropic and hence are characterized by two independent moduli. Here we compute the upper bounds on the effective bulk moduli of these structures using the cross-property bound (44) and the shear moduli

of the Delaunay networks using the bounds (45) and (46). The results are summarized in Table 4. It is noteworthy that similar to the conduction problem, as both short-range and long-range order of the network increases, the effective bulk moduli of all the networks and the shear moduli of the Delaunay networks increase. Specifically, when $\chi = 0.49$, the corresponding statistically isotropic stealthy networks possess nearly optimal effective bulk moduli, and the Delaunay ones among them possess nearly optimal effective shear moduli as well.

Table 4. Upper bounds on the effective moduli K_e , G_e , and E_e of the various isotropic disordered networks summarized in Table 3 and shown in Figs. 7 and 8. Here the effective properties are scaled by the corresponding moduli K , G , E , and volume fraction ϕ of the “channel” phase. The results are averaged over ten configurations for each system. The results for G_e and E_e are only shown for Delaunay networks. Note that disordered statistically isotropic stealthy cellular networks with $\chi = 0.49$ possess nearly optimal bulk moduli.

Point pattern	Tessellation	$K_e/(K\phi)$	$G_e/(G\phi)$	$E_e/(E\phi)$
Poisson	Delaunay	$0.4643(1 - \nu)$	$0.2322(1 + \nu)$	0.3095
Poisson	Voronoi	$0.4473(1 - \nu)$		
Poisson	Delaunay-centroidal	$0.4490(1 - \nu)$		
RSA	Delaunay	$0.4860(1 - \nu)$	$0.2430(1 + \nu)$	0.3240
RSA	Voronoi	$0.4907(1 - \nu)$		
RSA	Delaunay-centroidal	$0.4859(1 - \nu)$		
MRJ	Delaunay	$0.4887(1 - \nu)$	$0.2444(1 + \nu)$	0.3258
MRJ	Voronoi	$0.4971(1 - \nu)$		
MRJ	Delaunay-centroidal	$0.4890(1 - \nu)$		
Stealthy with $\chi = 0.3$	Delaunay	$0.4698(1 - \nu)$	$0.2349(1 + \nu)$	0.3132
Stealthy with $\chi = 0.3$	Voronoi	$0.4842(1 - \nu)$		
Stealthy with $\chi = 0.3$	Delaunay-centroidal	$0.4677(1 - \nu)$		
Stealthy with $\chi = 0.4$	Delaunay	$0.4751(1 - \nu)$	$0.2376(1 + \nu)$	0.3167
Stealthy with $\chi = 0.4$	Voronoi	$0.4896(1 - \nu)$		
Stealthy with $\chi = 0.4$	Delaunay-centroidal	$0.4762(1 - \nu)$		
Stealthy with $\chi = 0.49$	Delaunay	$0.4937(1 - \nu)$	$0.2469(1 + \nu)$	0.3291
Stealthy with $\chi = 0.49$	Voronoi	$0.4984(1 - \nu)$		
Stealthy with $\chi = 0.49$	Delaunay-centroidal	$0.4952(1 - \nu)$		

7. Conclusion and Discussion

In this work, we considered and constructed various 2D ordered and disordered low-density cellular networks, and determined their effective conductivities, tortuos-

ity tensors, and elastic moduli. In particular, we investigated periodic hyperuniform networks including both macroscopically isotropic and anisotropic varieties, as well as various disordered statistically isotropic net-

works derived from Voronoi, Delaunay, and “Delaunay-centroidal” tessellations based on hyperuniform and nonhyperuniform point patterns. We observed that the presence of “dead ends” in a network leads to suboptimal effective conductivity. We also demonstrated for the first time that intersecting parallel-channel cellular networks, including disordered hyperuniform and nonhyperuniform varieties, possess optimal effective conductivity tensors. We find that the effective conductivities and elastic moduli of the disordered Voronoi, Delaunay, and “Delaunay-centroidal” networks correlated positively with the short-range and long-range order of the networks, which is consistent with the fact that Poisson networks have the lowest effective properties due to the absence of any order. Moreover, we found that certain disordered networks derived from disordered stealthy hyperuniform point patterns with χ values just below $1/2$ maximize heat (or electrical) conduction/dissipation and fluid transport through the solid phase, and are capable of sustaining external stress with minimal amount of deformation. The Delaunay ones among them possess nearly optimal effective shear moduli as well. In summary, the effective transport and elastic properties of disordered networks derived from stealthy point patterns generally improve as the short-range order increases due to an increasing value of χ within the disordered regime ($\chi < 1/2$). This is also supported by a previous study [28] in which the size of the photonic band gap of a disordered stealthy hyperuniform dielectric network was shown to be proportional to χ .

It should not go unnoticed that all of the results that we have obtained for the effective conductivity apply as well to the fluid permeability associated with slow viscous flow through the channels. This is because the Stokes-flow equations for fluid transport in networks in the low-density limit ($\phi \rightarrow 0$) become identical to the conduction governing equations [1]. Thus, networks that are optimal with respect to the effective conductivity are also optimal with respect to the fluid permeability. Moreover, because the fluid permeability has been shown to be directly linked to the mean survival time associated with diffusion-controlled reactions in channels [58], our results for the effective conductivity are also optimal for the mean survival time.

The variety of favorable properties make these low-weight networks ideal for applications that require multifunctionality with respect to transport, mechanical and electromagnetic properties, e.g., aerospace applications [59]. Such low-weight multifunctional networks can be readily fabricated using 3D printing and lithographic technologies [60, 61]. In addition, although the procedures and results in this work focused on two dimensions, they can be easily extended

to treat three-dimensional open-cell foams, where the void phase is interconnected, which may have potential biomedical applications [62].

While the identified optimal networks were derived in the low-density limit ($\phi \rightarrow 0$), we expect that they remain optimal for small but positive volume fractions and may even apply at intermediate values of ϕ when the channels are “thickened.” Previous work described in Refs. [18, 19] supports this conjecture. Confirming this conjecture represents a worthy subject for future research.

It is useful to note that disordered networks derived from disordered hyperuniform point patterns are not necessarily hyperuniform. This is related to the fact that the centroids of the polygons in the disordered network do not necessarily coincide with the points in the disordered point pattern that is used to generate the network [63]. A previous numerical study of dielectric networks derived from stealthy point configurations [29] strongly suggests that these networks are also stealthy and hyperuniform. However, the rigorous mathematical conditions required to transform stealthy hyperuniform point patterns into stealthy hyperuniform networks have yet to be identified. By contrast, ordered networks derived from ordered hyperuniform point patterns are always hyperuniform. For example, the honeycomb network associated with the Voronoi tessellations of the hyperuniform point pattern of triangular lattice is hyperuniform. Moreover, the spectral density of the honeycomb network $[\tilde{\chi}_v(\mathbf{k})]_H$ is proportional to the structure factor of the triangular lattice $[S(\mathbf{k})]_T$, i.e.,

$$[\tilde{\chi}_v(\mathbf{k})]_H = \rho \tilde{m}^2(\mathbf{k}) [S(\mathbf{k})]_T, \quad (68)$$

where ρ is the number density of the triangular lattice, and $\tilde{m}(\mathbf{k})$ is the Fourier transform of the indicator function of the material in the fundamental cell (the smallest repeating hexagonal unit) of the honeycomb network. The investigation of the relationship between the hyperuniformity of disordered point patterns and the hyperuniformity of the generated disordered network could shed light on identifying novel ways to generate disordered hyperuniform networks.

Acknowledgments

The authors gratefully acknowledge the support of the Air Force Office of Scientific Research Program on Mechanics of Multifunctional Materials and Microsystems under Award No. FA9550-18-1-0514.

References

- [1] Torquato S 2002 Random Heterogeneous Materials: Microstructure and Macroscopic Properties (Springer-Verlag, New York)
- [2] Sahimi M 2003 Heterogeneous Materials I: Linear transport and optical properties vol 1 (Springer, New York)
- [3] Torquato S, Hyun S and Donev A 2002 Multifunctional composites: optimizing microstructures for simultaneous transport of heat and electricity Phys. Rev. Lett. **89** 266601
- [4] Torquato S and Donev A 2004 Minimal surfaces and multifunctionality Proc. Royal Soc. A **460** 1849–1856
- [5] Zohdi T I 2012 Electromagnetic properties of multiphase dielectrics: a primer on modeling, theory and computation vol 64 (Springer, New York)
- [6] Gibson L J and Ashby M F 1999 Cellular solids: structure and properties (Cambridge university press)
- [7] Wadley H N G 2006 Multifunctional periodic cellular metals Philos. Trans. R. Soc. A **364** 31–68
- [8] Valdevit L, Jacobsen A J, Greer J R and Carter W B 2011 Protocols for the optimal design of multifunctional cellular structures: From hypersonics to micro-architected materials J. Am. Ceram. Soc. **94** s15–s34
- [9] Berger J B, Wadley H N G and McMeeking R M 2017 Mechanical metamaterials at the theoretical limit of isotropic elastic stiffness Nature **543** 533–537
- [10] Sun H, Xu Z and Gao C 2013 Multifunctional, ultra-flyweight, synergistically assembled carbon aerogels Adv. Mater. **25** 2554–2560
- [11] Sun Y, Chen Q and Pugno N 2014 Elastic and transport properties of the tailorable multifunctional hierarchical honeycombs Compos. Struct. **107** 698–710
- [12] Zheng X, Lee H, Weisgraber T H, Shusteff M, DeOtte J, Duoss E B, Kuntz J D, Biener M M, Ge Q, Jackson J A et al. 2014 Ultralight, ultra-stiff mechanical metamaterials Science **344** 1373–1377
- [13] Wicklein B, Kocjan A, Salazar-Alvarez G, Carosio F, Camino G, Antonietti M and Bergström L 2015 Thermally insulating and fire-retardant lightweight anisotropic foams based on nanocellulose and graphene oxide Nat. Nanotechnol. **10** 277–283
- [14] Iyer S, Alkhalid M and Venkatesh T A 2015 Electromechanical behavior of auxetic piezoelectric cellular solids Scr. Mater. **99** 65–68
- [15] Durand M and Weaire D 2004 Optimizing transport in a homogeneous network Phys. Rev. E **70** 046125
- [16] Durand M 2005 Optimizing the bulk modulus of low-density cellular networks Phys. Rev. E **72** 011114
- [17] Lu T J, Stone H A and Ashby M F 1998 Heat transfer in open-cell metal foams Acta Mater. **46** 3619–3635
- [18] Hyun S and Torquato S 2000 Effective elastic and transport properties of regular honeycombs for all densities J. Mater. Res. **15** 1985–1993
- [19] Hyun S and Torquato S 2002 Optimal and manufacturable two-dimensional, kagome-like cellular solids J. Mater. Res. **17** 137–144
- [20] Torquato S and Stillinger F H 2003 Local density fluctuations, hyperuniformity, and order metrics Phys. Rev. E **68** 041113
- [21] Zachary C E and Torquato S 2009 Hyperuniformity in point patterns and two-phase random heterogeneous media J. Stat. Mech. Theor. Exp. **2009** P12015
- [22] Torquato S 2018 Hyperuniform states of matter Phys. Rep. **745** 1–95
- [23] Torquato S 2016 Hyperuniformity and its generalizations Phys. Rev. E **94** 022122
- [24] Torquato S 2016 Disordered hyperuniform heterogeneous materials J. Phys. Condens. Matter **28** 414012
- [25] Chen D and Torquato S 2018 Designing disordered hyperuniform two-phase materials with novel physical properties Acta Mater. **142** 152–161
- [26] Zhang G, Stillinger F H and Torquato S 2016 Transport, geometrical, and topological properties of stealthy disordered hyperuniform two-phase systems J. Chem. Phys. **145** 244109
- [27] Xu Y, Chen S, Chen P, Xu W and Jiao Y 2017 Microstructure and mechanical properties of hyperuniform heterogeneous materials Phys. Rev. E **96** 043301
- [28] Florescu M, Torquato S and Steinhardt P J 2009 Designer disordered materials with large, complete photonic band gaps Proc. Natl. Acad. Sci. U.S.A. **106** 20658–20663
- [29] Man W, Florescu M, Williamson E P, He Y, Hashemizad S R, Leung B Y C, Liner D R, Torquato S, Chaikin P M and Steinhardt P J 2013 Isotropic band gaps and freeform waveguides observed in hyperuniform disordered photonic solids Proc. Natl. Acad. Sci. U.S.A. **110** 15886–15891
- [30] Florescu M, Steinhardt P J and Torquato S 2013 Optical cavities and waveguides in hyperuniform disordered photonic solids Phys. Rev. B **87** 165116
- [31] DeglInnocenti R, Shah Y D, Masini L, Ronzani A, Pitanti A, Ren Y, Jessop D S, Tredicucci A, Beere H E and Ritchie D A 2016 Hyperuniform disordered terahertz quantum cascade laser Sci. Rep. **6** 19325
- [32] Leseur O, Pierrat R and Carminati R 2016 High-density hyperuniform materials can be transparent Optica **3** 763–767
- [33] Gkantzounis G, Amoah T and Florescu M 2017 Hyperuniform disordered phononic structures Phys. Rev. B **95** 094120
- [34] Muller N, Haberko J, Marichy C and Scheffold F 2017 Photonic hyperuniform networks obtained by silicon double inversion of polymer templates Optica **4** 361–366
- [35] Zhang G, Stillinger F H and Torquato S 2017 Can exotic disordered stealthy particle configurations tolerate arbitrarily large holes? Soft Matter **13** 6197–6207
- [36] Torquato S 2010 Reformulation of the covering and quantizer problems as ground states of interacting particles Phys. Rev. E **82** 056109
- [37] Torquato S, Zhang G and Stillinger F H 2015 Ensemble theory for stealthy hyperuniform disordered ground states Phys. Rev. X **5** 021020
- [38] Uche O U, Stillinger F H and Torquato S 2004 Constraints on collective density variables: Two dimensions Phys. Rev. E **70** 046122
- [39] Zhang G, Stillinger F H and Torquato S 2015 Ground states of stealthy hyperuniform potentials: I. Entropically favored configurations Phys. Rev. E **92** 022119
- [40] Dreyfus R, Xu Y, Still T, Hough L A, Yodh A G and Torquato S 2015 Diagnosing hyperuniformity in two-dimensional, disordered, jammed packings of soft spheres Phys. Rev. E **91** 012302
- [41] Milton G W 2002 The Theory of Composites (Cambridge University Press, Cambridge, England)
- [42] Sen A K and Torquato S 1989 Effective conductivity of anisotropic two-phase composite media Phys. Rev. B **39** 4504
- [43] Torquato S 1997 Effective stiffness tensor of composite media: exact series expansions J. Mech. Phys. Solids **45** 1421–1448
- [44] Willis J R 1977 Bounds and self-consistent estimates for the overall properties of anisotropic composites J. Mech. Phys. Solids **25** 185
- [45] Milton G W and Golden K 1985 Thermal conduction in composites 18th International Thermal Conductivity Conference (New York: Plenum Press)
- [46] Bergman D J 1980 Exactly solvable microscopic geometries and rigorous bounds for the complex dielectric constant

- of a two-component composite material Phys. Rev. Lett. **44** 1285
- [47] Milton G W 1981 Bounds on the complex permittivity of a two-component composite material J. Appl. Phys. **52** 5286
- [48] Tartar L 1985 Estimations fines des coefficients homogénéisés Ennio De Giorgi's Colloquium ed Krée P (Boston: Pitman)
- [49] Vigdergauz S B 1989 Regular structures with extremal elastic properties Mech. Solids **24** 57–63
- [50] Vigdergauz S B 1994 Two-dimensional grained composites of extreme rigidity J. Appl. Mech. **61** 390
- [51] Gibiansky L V and Torquato S 1993 Link between the conductivity and elastic moduli of composite materials Phys. Rev. Lett. **71** 2927
- [52] Gibiansky L V and Torquato S 1996 Connection between the conductivity and bulk modulus of isotropic composite materials Proc. R. Soc. Lond. A **452** 253–283
- [53] Torquato S, Gibiansky L V, Silva M J and Gibson L J 1998 Effective mechanical and transport properties of cellular solids Int. J. Mech. Sci. **40** 71–82
- [54] Matyka M, Khalili A and Koza Z 2008 Tortuosity-porosity relation in porous media flow Phys. Rev. E **78** 026306
- [55] Lu T J and Chen C 1999 Thermal transport and fire retardance properties of cellular aluminium alloys Acta Mater. **47** 1469–1485
- [56] Zhang G and Torquato S 2013 Precise algorithm to generate random sequential addition of hard hyperspheres at saturation Phys. Rev. E **88** 053312
- [57] Atkinson S, Stillinger F H and Torquato S 2014 Existence of isostatic, maximally random jammed monodisperse hard-disk packings Proc. Natl. Acad. Sci. U.S.A. **111** 18436–18441
- [58] Torquato S 1990 Relationship between permeability and diffusion-controlled trapping constant of porous media Phys. Rev. Lett. **64** 2644
- [59] Noor A K, Venneri S L, Paul D B and Hopkins M A 2000 Structures technology for future aerospace systems Comput. Struct. **74** 507–519
- [60] Vaezi M, Seitz H and Yang S 2013 A review on 3D micro-additive manufacturing technologies Int. J. Adv. Manuf. Technol. **67** 1721–1754
- [61] Compton B G and Lewis J A 2014 3D-printing of lightweight cellular composites Adv. Mater. **26** 5930–5935
- [62] Hutmacher D W 2000 Scaffolds in tissue engineering bone and cartilage Biomaterials **21** 2529–2543
- [63] Klatt M A, Lovric J, Chen D, Kapfer S C, Schaller F M, Schoenhofer P W A, Gardiner B S, Smith A S, Torquato S and Schroeder-Turk G E Universal hidden order in amorphous cellular geometries (submitted for publication)